# Atom Probe Tomography of Apatites and Bone-Type Mineralized Tissues

Lyle M. Gordon, Lawrence Tran, and Derk Joester*

Northwestern University, Department of Materials Science and Engineering, 2220 Campus Drive, Evanston, Illinois 60208, United States

ABSTRACT Nanocrystalline biological apatites constitute the mineral phase of vertebrate bone and teeth. Beyond their central importance to the mechanical function of our skeleton, their extraordinarily large surface acts as the most important ion exchanger for essential and toxic ions in our body. However, the nanoscale structural and chemical complexity of apatite-based mineralized tissues is a formidable challenge to quantitative imaging. For example, even energy-filtered electron microscopy is not suitable for detection of small quantities of low atomic number elements typical for biological materials. Herein we show that laser-pulsed atom probe tomography, a technique that combines subnanometer spatial resolution with unbiased chemical sensitivity, is uniquely suited to the task. Common apatite end members share a number

of features, but can clearly be distinguished by their spectrometric fingerprint. This fingerprint and the formation of molecular ions during field evaporation can be explained based on the chemistry of the apatite channel ion. Using end members for reference, we are able to interpret the spectra of bone and dentin samples, and generate the first three-dimensional reconstruction of 1.2×10^7 atoms in a dentin sample. The fibrous nature of the collagenous organic matrix in dentin is clearly recognizable in the reconstruction. Surprisingly, some fibers show selectivity in binding for sodium ions over magnesium ions, implying that an additional, chemical level of hierarchy is necessary to describe dentin structure. Furthermore, segregation of inorganic ions or small organic molecules to homophase interfaces (grain boundaries) is not apparent. This has implications for the platelet model for apatite biominerals.
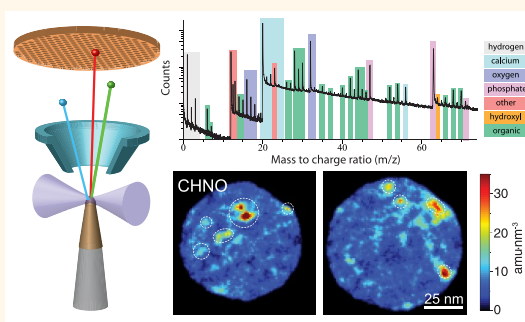
KEYWORDS: apatite · atom probe tomography · organic−inorganic interfaces · biomineralization · dentin · bone

Nanocrystalline apatite is the mineral phase in bone, dentin, and enamel. It provides stiffness, strength, wear resistance, and forms part of a hierarchical, high-toughness, low-density composite with collagen and other proteins.[1−3] The biomineral in vertebrate bone and teeth resembles hydroxylapatite (OHAp), one of the apatite end members. The other common end members are fluorapatite (FAp), and chlorapatite (ClAp). OHAp, ClAp, and FAp share the same general composition $Ca_{10}(PO_4)_6(OH,F,Cl)_2$[4,5] and exhibit a nearly identical crystal structure (Figure 1).[6] Substituents in the apatite lattice alter the structure and stoichiometry, introduce vacancies, modulate physiochemical properties of the mineral, and are of importance for applications from biomaterials to phosphors and high-energy lasers.[7,8]

While apatite is sparingly soluble at physiological pH, the bone mineral surface (>500 000 m^2 in an average human) is in rapid exchange with ionic species present in solution, thus acting as a sorbent and ion-exchanger in contact with body fluids.[11]

Bone apatite is substituted with significant amounts of carbonate and provides a reservoir of essential ions for biological functions, including calcium, magnesium, and sodium.[9,12−17] Certain species (*e.g.*, F−, Al^{3+}, Sr^{2+}, bisphosphonates) accumulate in bone, where they can alter mineral solubility and crystallite size, interfere with collagen-mineral bonding, and affect bone cells. This can be advantageous, for example, fluoride reducing the susceptibility of enamel to caries,[18] or detrimental, as in skeletal fluorosis[19] or in aluminum-induced bone disease.[20]

Despite the importance of the interfacial processes occurring at the surface of apatite nanocrystals, our understanding of structure, chemical composition, and bonding across the interface is rather limited. This is at least in part due to the small length scale, complex three-dimensional structure, and hard/soft hybrid nature that complicate quantitative imaging. Despite recent progress in atomic resolution elemental mapping by electron energy loss spectroscopy (EELS) or energy dispersive X-ray spectroscopy (EDS) in
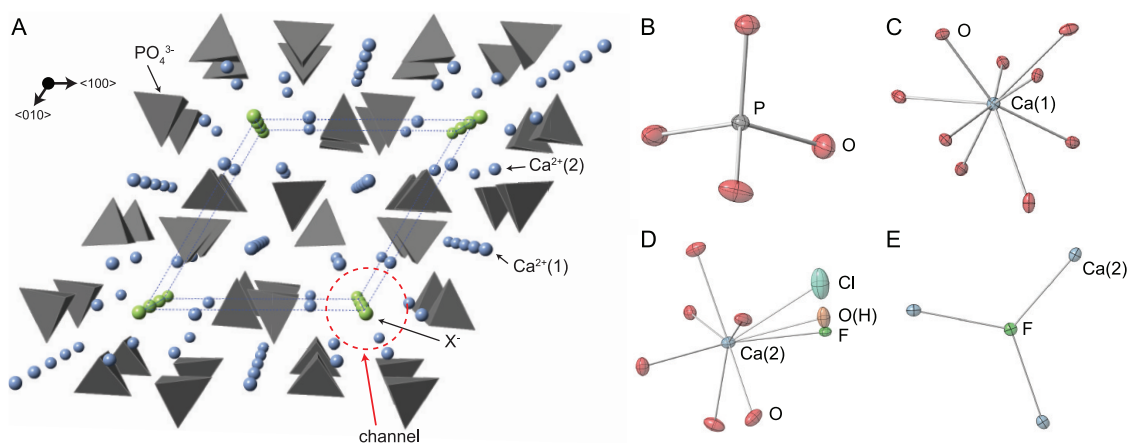
Figure 1. Apatite crystal structure. (A) The apatite unit cell with four distinct crystallographic positions (sites): six tetrahedral phosphates **(B)**; four Ca(1) coordinated by nine oxyanions **(C)**; six Ca(2) coordinated by six oxyanions and one channel ion **(D)**; and two channel sites, which are occupied by F^-, OH^-, or Cl^- and are coordinated by three Ca(2) **(E)**.[9] The Ca(2) site shows the channel ion positions from the FAp, ClAp, and OHAp crystal structures.[10] While unit cell parameters change slightly and the symmetry of the crystal is affected by the position of the channel ion, the structures are highly similar. Thermal ellipsoids were rendered according to the atom-specific anisotropic thermal parameters at 80% probability level.

scanning transmission electron microscopy (STEM), the resolution and chemical sensitivity in biological minerals are greatly limited by the susceptibility of these materials to electron beam damage. Furthermore, many physiological ions with low atomic number have unfavorable spectroscopic properties that can make quantification very difficult or impossible.

We have recently shown that atom probe tomography (APT), an imaging mass spectrometry technique, may rise to the challenge.[21,22] APT is based on the phenomenon of field evaporation, where ions successively desorb from a microtip in the presence of an electric field.[23] The chemical identity of each ion is determined by time-of-flight mass spectrometry. APT is capable of simultaneously mapping the structure and composition of nanoscale volumes ($10^5 - 10^6$ nm^3) with subnanometer spatial resolution and parts-per-million (ppm) chemical sensitivity.[23,24] The advent of laser-pulsed APT has widened the scope of the technique to include a range of dielectric materials, including a small number of biological and geological minerals.[21,25−28] We show here that APT is well suited for the analysis of apatite-based materials by investigating spectral features of synthetic and geological apatite end members. We then expand our spectral analysis to vertebrate bone and dentin as examples for apatite-mineralized tissues that contain a range of inorganic substituents and organic molecules. Finally, we discuss preliminary data showing that APT captures the fibrous nature of the collagenous organic matrix and reveals additional detail regarding the chemical nanostructure of homophase and heterophase interfaces.

RESULTS AND DISCUSSION

Crystallinity and phase purity of synthesized apatite single crystals were verified by X-ray diffraction, Raman

spectroscopy and Fourier transform infrared spectroscopy (see Supporting Information, Figures 5−9). The primary difficulties encountered in APT of low conductive, composite materials are (a) developing appropriate sample preparation protocols and (b) finding APT operational parameters that minimize sample failure while optimizing the quality of spectra and reconstructions. APT samples were prepared by focused ion beam (FIB) milling. We identified operational parameters (laser pulse energy P_e = 150 pJ, laser pulse frequency P_f = 200 kHz) for APT of synthetic OHAp in a systematic study of the influence of laser pulse energy and laser pulse frequency on background level, spectral resolution, and the accuracy of the measured compositions as indicators of data quality (Supporting Information, Figure 1). Apatite mass spectra indicate the formation Ca^{2+}, O_2^{2+}/O_2^+, and $P_xO_y^+$ cluster ions during field evaporation (Figure 2). In addition, the channel ions give rise to characteristic spectral features. Elements that typically substitute in bone apatite, including Mg^{2+}, Na^+, and Sr^{2+}, and trace amounts of $^{69}Ga^+$ implanted during FIB-based sample preparation, were also detected.

The stoichiometry of the apatite samples (Table 1) agrees reasonably well with predictions for OHAp and ClAp. However, the amount of oxygen is lower and the amount of phosphorus is higher than predicted. This error is relatively small for OHAp and ClAp, but more pronounced in FAp. As the Ca/P ratio is sensitive to instrumental parameters, run time parameters for FAp could likely be optimized. At this time, it is not clear why the stoichiometry of FAp as determined by APT deviates significantly from that of the other apatites.

In atom probe spectra of metals and elemental semiconductors, monatomic ions predominate. Spectra of compound semiconductors and dielectrics include numerous molecular ions. However, the process
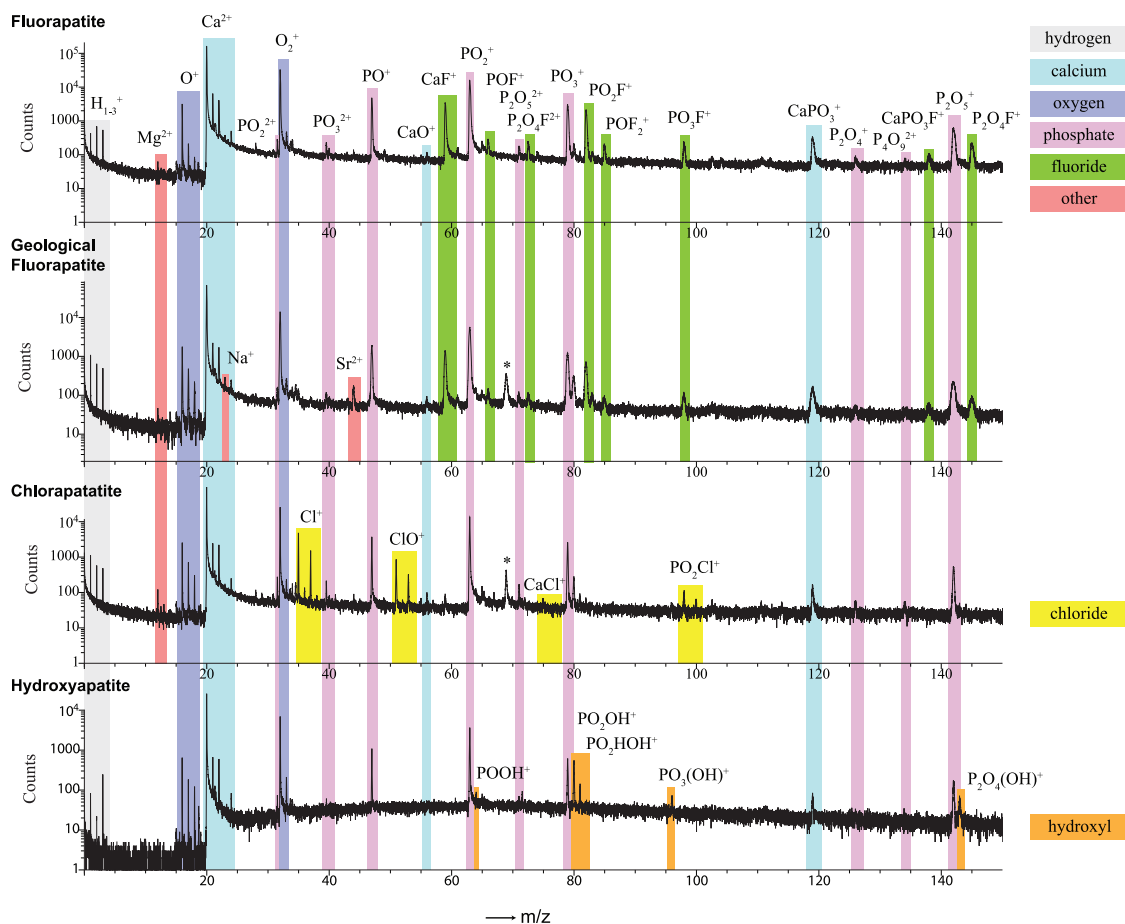
Figure 2. APT spectra of synthetic and geological apatites: Ions common to all apatites include Ca^{2+} and $CaPO_3^+$ (light blue), O^+/O_2^{2+} and O_2^+ (purple), a variety of $P_xO_y^{n+}$ clusters (pink) and H_x^+ species (light gray). End members give rise to characteristic ions such as CaF^+ and $P_xO_yF_n^+$ in FAp (green), Cl^+, ClO^+, and PO_2Cl^+ in ClAp (yellow), and $P_xO_y(OH)^+$ in OHAp (orange). FIB-implanted Ga (∗) and other low-level inorganic substituents (red) are also detected. For a comprehensive list of ions formed, including those with mass-to-charge ratios >150, please see Supporting Information Table 1 and Figure 2.

TABLE 1. APT Compositional Measurements of Apatites

| sample | mole fraction (atomic %) | | | | | |
	Ca	P	Ca/P	O/P	O	X
calcd (OHAp)	22.7	13.6	1.66	4.13	59.1	4.55 (X = H)
calcd (FAp/ClAp)	23.8	14.3	1.66	3.99	57.1	4.8 (X = F/Cl)
OHAp	23.8	16.9	1.41	3.33	56.4	2.9 (X = H)
FAp	30.7	15.6	1.97	3.20	49.9	3.6 (X = F)
geoFAp	31.5	14.3	2.20	3.47	49.6	3.1 (X = F)
ClAp	24.7	16.3	1.52	3.36	54.7	2.9 (X = Cl)

Figure 3. The relative abundance of $P_xO_y^+$ ions in apatite spectra differs from that of Fe^{2+}/FeO_x^+ ions in magnetite.[21] The error bars indicate the standard deviation of the data across four synthetic and geologic apatites (OHAp, ClAp, FAp, geoFAp). The magnetite data are from a single data set obtained from a geologic single crystal.[21]

of field evaporation and molecular ion formation in dielectric materials remains poorly understood. Inspection of apatite spectra reveals that calcium, which forms primarily ionic bonds, has a markedly different propensity to form molecular ions than the covalently bound phosphorus. In addition, differences in the chemical nature of the channel ion lead to characteristic spectral fingerprints of the structurally nearly identical apatite end members.

In apatite spectra, phosphorus occurs in molecular ions ranging in size from PO^+ to $P_4O_{10}^+$ (Figure 3, Supporting Information Table 1). The relative abundance

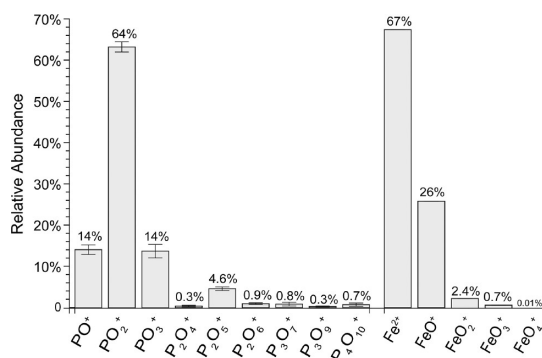of the fragments increases from PO^+ (13−16%) to PO_2^+ (63−64%) and then decays to PO_3^+ (13−16%). No monatomic $P^{+/2+}$ was detected. These relative abundances are in contrast to spectra of metal oxides, for example magnetite (Fe_3O_4), where the monatomic metal ion (Fe^{2+}) is the most abundant (67.4%), and the

relative abundance of ion type decreases with the number of oxygen atoms in the cluster (Figure 3). The phosphate P−O bond is clearly more robust under atom probe conditions than typical M−O bonds in transition metal oxides. This may be rationalized by considering the stabilization of the P−O bond by resonance (mesomerism) and its greater covalent nature (P−O, 61% *vs* Fe−O, 49%) based on Pauling electronegativity values.[29]

The Ca−O bond, on the other hand, is much less robust. Nearly all calcium was detected as Ca^{2+} with only a trace amount of CaO^+ apparent in spectra and less than 1% $CaPO_3^+$ (Supporting Information, Figure 3), where oxygen likely bridges between Ca and P. Clearly, when phosphorus and calcium compete for oxygen, phosphorus wins in the vast majority of cases. This may be a consequence of the lesser covalent nature of the Ca−O bond (21%) and the reduced ability of calcium to engage in *d*-orbital-mediated, ligand-to-metal charge-transfer.

While the channel ions share a similar environment, they give rise to characteristic sets of spectral features (Figure 2, Supporting Information, Table 1). Fluoride in FAp occurs as CaF^+ (47%), PO_2F^+ (36%), and a number of $P_xO_yF_z^+$ ions with lower abundance (total: 17%). ClAp spectra indicate that chloride, unlike fluoride, readily forms a monatomic ion (Cl^+, 76%) and ClO^+ (21%). The propensity of chloride to form molecular ions with phosphorus is significantly smaller (PO_2Cl^+, <3%). The fingerprint of OHAp consists of a series of ions of the general form $P_xO_y(OH)_z^+$, primarily $PO_2(OH)^+$, which accounts for 63% of all detected hydroxyl groups. While these ions could in principle form by recombination of phosphorus and oxygen-containing ions with residual hydrogen in the vacuum system, their absence in ClAp and FAp spectra indicates that they indeed form from the channel ion. However, the fingerprint peaks represent only 48% of the predicted number of hydroxyl ions. It is likely that the remaining hydroxyl groups evaporate as H_x^+ and $O_xH_y^+$ ions or potentially neutral atomic or molecular hydrogen, which go undetected.

The Ca−F bond, despite its weakly covalent character (9%), is surprisingly robust and accounts for ∼5% of the Ca ions and ∼47% of the fluoride in FAp. In comparison, only trace amounts of $CaCl^+$ ions were formed from ClAp, and $CaOH^+$ was not observed in OHAp. This is likely a consequence of the high electron affinity and first ionization potential of fluorine that also limits formation of the F^+ and FO^+ species. Chloride, on the other hand, is readily oxidized to Cl^+ and ClO^+; oxyanions and hydroxyl groups give rise to O^+ or pick up a proton and evaporate as OH^+. The abundance of $P_xO_yX_z^+$ clusters follows the same trend as the P−X bond strength, that is, P−O > P−F > P−Cl. The tendency of chloride to oxidize further reduces the likelihood for the formation of such clusters.

Larger molecular ions of the formula, $P_xO_yX_z^+$ do not represent discrete fragments of the apatite crystal lattice, as the phosphate tetrahedra are not vertex or edge linked and do not lie within bonding distance of the channel ion. The formation of these ions implies that atoms/ions have some mobility and can react to form larger ions (for an example of surface diffusion during APT of metals, see ref 30). Chemical intuition predicts that a reaction would occur by nucleophilic attack of an "X^-" species (*e.g.*, F^-) on an electrophilic phosphorus atom. If X^- has a limited lifetime because of competing processes (*e.g.*, oxidation to form X^+), this attack is less likely to occur. Whether the reaction occurs *via* nucleophilic attack is what actually happens under the extremely high electric field at the tip of the sample is not known. Regardless, a fluoride atom has to move at least 0.21 nm off its lattice position to reach the bonding distance of a phosphorus ion, and the formation of an O-bridged P_2O_x cluster requires that a distance of 0.17 nm be closed. While surface diffusion and the formation of clusters reduces the resolution of the compound's reconstruction by a small amount,[31] these molecular ions account for only ∼2−3% of the total ions, and they are homogeneously distributed within the reconstruction. It is thus unlikely that large molecular ions lead to artifacts that could affect interpretation of the data.

Bone and dentin are hierarchically structured materials with three major components, apatite (∼72 wt % of dry, defatted material), organics (∼20 wt %), and water.[32,33] The mineral phase best resembles OH-deficient OHAp substituted with significant carbonate (5−8 wt %) and smaller levels of Na^+ and Mg^{2+} (0.5−1.0 wt %).[9,11,33,34] Approximately 1 wt % of the composite is citrate ($C_6H_5O_7^{3-}$) that may be associated with the mineral surface and/or the collagen fibrils that constitute the majority of the organic fraction.[16,35] The poorly crystalline mineral is thought to be present in irregular platelets approximately $50 \cdot 25 \cdot 2-5$ nm^3 in size.[36,37] In forming bone and mineralizing tendon, these platelets are roughly aligned with their crystallographic *c*-axis parallel to collagen fibrils.[38] Within a fibril, platelets are generally parallel to each other. However, with increasing age, as the amount of intrafibrillar and interfibrillar mineral increases and platelets grow, the orientation of platelets with respect to each other becomes less homogeneous.[39−41]

To establish whether APT of bone-type materials is feasible, we analyzed samples prepared from rat femur cortical bone and elephant tusk dentin (ivory). As mechanically weak interfaces and the presence of organics can lead to sample failure during APT, we used FIB milling to lift out samples such that the collagen fibril direction was aligned with the long axis of the tip. Consistent with expectations, the resulting spectra (Figure 4, Supporting Information Figure 4) are similar to those of synthetic OHAp (Figure 2), with Mg^{2+} (0.5−1.7 atom %) and Na^+ (0.25−0.6 atom %)
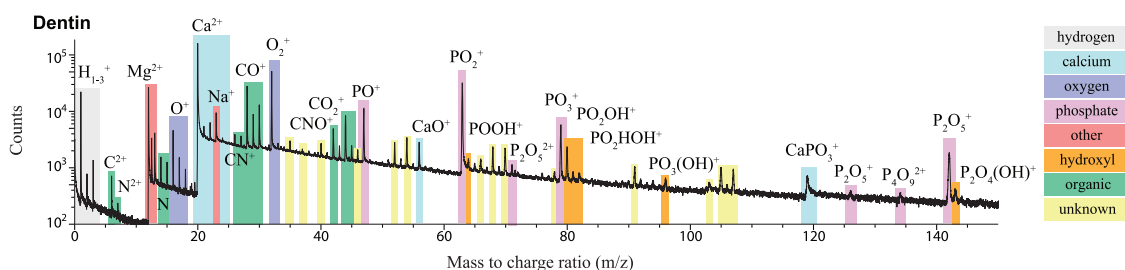
Figure 4. Spectrum of elephant tusk dentin highlighting the hydrogen, calcium, oxygen, phosphate, other inorganic ions, identified organic molecular fragments, the spectral signature of OHAp and a number of unidentified molecular ions likely corresponding to organic molecule fragments.
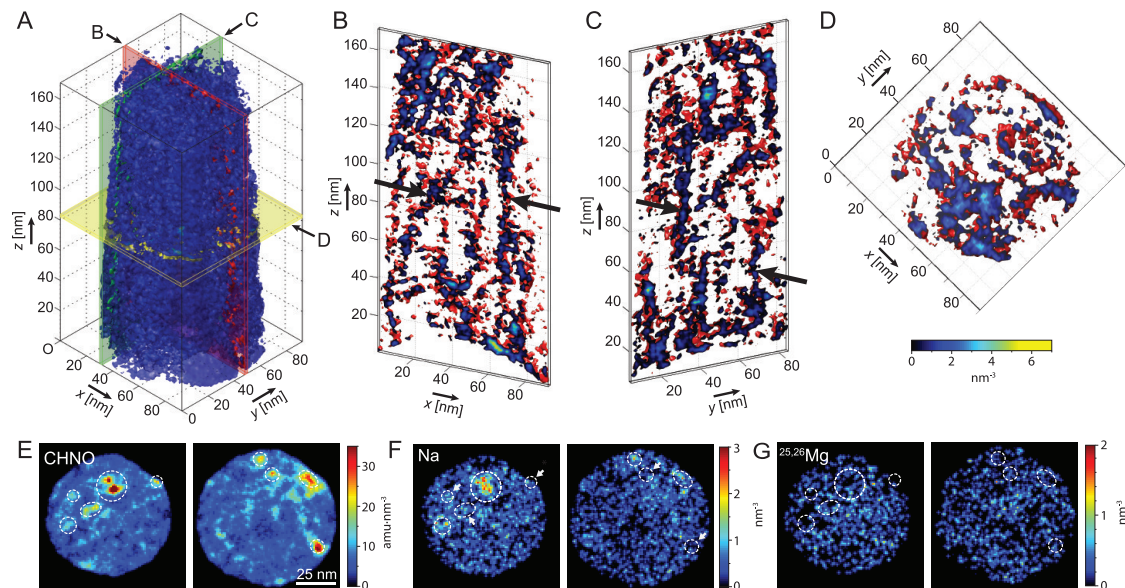

Figure 5. 3D reconstruction of a sample of elephant tusk dentin. (A) Isosurface (blue) of the number density of organic fragment ions (1.4 nm^{-3}, ions listed in Supporting Information Table 2). (B−D) Slices through the reconstructed volume parallel to the *XZ* plane (B), *YZ* plane (C), and *XY* plane (D). Isosurfaces (1.4 nm^{-3}) are rendered in red. End-caps[48] show the organic fragment number density. In B and C, a high density of organic fibers oriented roughly parallel to the *z*-axis (black arrows) is apparent. Fiber spacing is generally larger in the *XZ* plane than in the *YZ* plane. (E−G). Elemental maps generated from 5 nm thick slices parallel to the *XY* plane (left, *z* = 147−151 nm; right, *z* = 47−51 nm) showing mass density of organics (E) number density of Na$^+$, and number density of Mg^{2+}. Some organic fibers (dashed ellipses), but not all (white arrows), colocalize with sodium. Mg^{2+} is evenly distributed across the entire slice. Note that the Mg maps comprise only the minor isotopes (^{25}Mg, ^{26}Mg). On the basis of the natural abundances, we estimate that ions at *m/z* = 12 comprise 34% C$^+$ and 66% ^{24}Mg^{2+} while the totals of the ions at *m/z* = 12.5 and 13 consist only of 14% CH$^+$ (at *m/z* =13).

as substituents. Additional features include peaks corresponding to C$^{+/2+}$, N$^{+/2+}$, molecular ions of the general formula C$_{1−4}$N$_{0−1}$O$_{1−2}$H$_{0−2}^+$, and presumably organic ions that we have not identified (Supporting Information Table 2). While we cannot distinguish which "CHO"-containing ions arise from carbonate, citrate, or collagen, the origin of nitrogen and of larger molecular ions must be organic macromolecules.[21,22,42] Given the small sample size and the heterogeneous nature of bone and dentin, the match between the expected and the experimentally determined stoichiometry is reasonable (Supporting Information Table 3).

Strikingly, in a reconstruction of an elephant tusk dentin sample, there are "CHNO"-rich fibers that run approximately parallel to the analytical *z*-direction (Figure 5), which corresponds to the long axis of the elephant tusk, and is the direction in which the

collagen fibrils are oriented.[39,43] The smallest organic features that can be distinguished in APT reconstructions have cross sections corresponding to collagen microfibrils consisting of 5 collagen triple helices (2.7·4 nm^2).[44] Larger assemblies are also apparent. We have not yet been able to identify features with the typical periodicity of hole and gaps zones of collagen.

Some, but not all, organic fibers colocalize with high sodium concentrations (Figure 5E). These fibers do not colocalize with magnesium ions, indicating that the binding is specific. We did not observe fibers that show selective binding of Mg^{2+} (Figure 5F). Cations are most likely bound by acidic amino acids or proteoglycans in the collagenous organic matrix. Specificity in binding implies that there are subtle differences in the organic fibers. For example, some fibers could contain a protein or proteoglycan that binds Na$^+$ specifically. This

could influence the charge density of such fibers, their self-assembly behavior, nucleation and growth of OHAp during mineralization, or the amount of water bound by the fiber, and thus its mechanical and self-healing properties. We first reported specific ion binding by fibers in the organic matrix of the chiton tooth.[21] Having observed such specificity in invertebrate mollusks and mammals, it is intriguing to think that a chemical level of hierarchy may be a general feature that controls self-assembly and/or functional properties of biomineralized tissues. Atom probe is currently the only technique that is able to detect chemical heterogeneity in biomaterials at this length scale.

While heterophase interfaces between organic fibers and the mineral can be readily identified in 3D maps of the organic fragment ion distribution, there are no features in reconstructions that correspond to homophase interfaces, that is, grain boundaries between crystallites. Furthermore, we see no evidence of segregation of Na^+ or Mg^{2+} to either grain boundaries or organic−inorganic interfaces. Instead, Na^+ and Mg^{2+} are nearly homogenously distributed throughout the mineral phase. This is in apparent contradiction to the current model of bone[9,41] and dentin,[40,45] including elephant dentin[39,46,47] that posits that apatite crystallites have irregular platelet habit and that organic and inorganic species, particularly citrate and magnesium, segregate to platelet surfaces, where they influence the biological properties of the material. There are three alternative explanations for this conundrum: (1) OHAp occurs in irregular shapes that correspond to the spaces between the organic fibrils (Figure 5B−D). The appearance of platelet shaped crystallites in TEM is an artifact. (2) Na^+ and Mg^{2+} do no segregate. There are platelets, but they cannot be recognized in APT reconstructions based on the Na or Mg distribution. (3) There are platelets, and Na^+ and Mg^{2+} do segregate, but interfaces cannot be resolved due to limitations of APT.

We have observed segregation of Na and Mg to interfaces in dental enamel (not shown), which argues against alternative 2. Analysis of small-angle X-ray scattering data does not necessarily agree with a platelet habit, arguing in favor of alternative 1.[11] We believe that a substantial amount of additional information will be required to arrive at a complete understanding of crystallite habit and interfacial segregation in different bone-type composites.

CONCLUSION

APT offers unrivaled spatial resolution and unbiased chemical sensitivity in compositionally and texturally complex materials. Laser pulsing enables the analysis of low conductivity materials. We have shown herein that apatites, a class of phosphate minerals with exceptional flexibility in accommodating substituents and of broad importance for multiple disciplines, are suitable for APT investigation. APT spectra of different apatite end members, including OHAp, FAp, and ClAp, show a common set of atomic and molecular ions but a unique spectrometric fingerprint specific to the channel ion. We can rationalize the preferential formation of atomic and cluster ions using simple concepts of electronegativity and bond strength. Simulations of the field evaporation process may help develop a quantitative understanding of the process.

Using the synthetic apatites for reference, we analyzed elephant tusk dentin and rat femur cortical bone as examples of structurally and chemically complex biological nanocomposites. Atom probe spectra clearly identify ions derived from organic matrix molecules. Reconstructions reveal fibrous organic structures that likely correspond to individual collagen microfibrils and their assemblies in elephant dentin. We observed specificity in ion binding for some fibers, indicating a previously unknown level of chemical hierarchy in the structure of dentin. This is the second example for chemical heterogeneity at the single-fiber level after our discovery in the chiton tooth, and may represent a widespread biological strategy in biomineralization. The functional significance of the observed specificity is not yet clear.

Current reconstructions do not reproduce the platelet habit of the OHAp crystallites. It is not clear whether this is a limitation of atom probe tomography,[49] whether platelets are an artifact of electron microscopy, or whether interfaces in bone materials are far more diffuse than the description as discrete platelets implies. We are optimistic that the structural and chemical information gleaned from electron microscopy, APT, and their correlative combination will enable a much-improved characterization of bone and other biomineralized tissues. Such analytical information, which has implications for our understanding of how organisms manipulate apatite structure and chemistry for different applications in bone, dentin, and enamel will help analyze pathological changes and provide a basis for the development of bioinspired nanocomposites.

MATERIALS AND METHODS

The following materials were used: hydroxyapatite (OHAp, $Ca_5(PO4)_3OH$, 99.995 wt %) powder, anhydrous calcium chloride ($CaCl_2$), beta-tricalcium phosphate ($Ca_3(PO_4)_2$), calcium fluoride (CaF_2), aluminum nitrate nonahydrate ($Al(NO_3)_3 \cdot 9H_2O$) (Sigma Aldrich, St. Louis, MO); potassium sulfate (K_2SO_4) (EMD, Darmstadt,

Germany); glutaraldehyde, sodium cacodylate (Electron Microscopy Sciences, Hatfield, PA); 5 mL alumina combustion boat, 25 mL alumina crucible, alumina crucible cover (Coors Tek, Golden, CO); 1 mL tungsten evaporation boat (R. D. Mathis, Long Beach, Ca); Epo-Fix resin (Struers, Cleveland, OH); LR White resin (London Resin Company, Aldermaston, Reading, Berkshire, UK); CarbiMet II SiC grinding paper, Metadi supreme polycrystalline aqueous

diamond polishing suspension, Microcloth polishing cloths (Buehler, Lake Bluff, IL); Conductive Liquid Silver Paint (Ted Pella, Redding, CA). Ultrapure water (ρ = 18.2 M$\Omega\cdot$cm) prepared with a Barnstead Nanopure UF+UV ultrapure water purification system (Thermo-Fisher Scientific, Waltham, MA); geological fluorapatite single crystals (Amongems, Bangkok, Thailand).

K_2SO_4 was purified twice by recrystallization. Specifically, 25 g of K_2SO_4 was dissolved in 200 mL of boiling water while stirring. The K_2SO_4 solution was vacuum filtered and the filtrate was transferred to an ice bath to precipitate the K_2SO_4. The precipitated K_2SO_4 was washed with acetone and dried in air at 120 °C.

Single Crystal Synthesis. OHAp single crystals were synthesized using a potassium sulfate flux.[50] Briefly, 2 g of high-purity OHAp powder was ground with a porcelain mortar and pestle and placed into a 5 mL alumina combustion boat. The sample was heated to 1000 °C (8.33 °C/min) and held at this temperature for 6 h in air to remove water and trace organic material. The powder was left to cool to room temperature in the furnace before it was mixed with K_2SO_4 at a K_2SO_4/OHAp weight ratio of 1.6:1 (1538 mg K_2SO_4:960 mg OHAp) with a porcelain mortar and pestle. The mixture was placed into a 5 mL alumina combustion boat, heated to 1150 °C (9.2 °C/min), and held at this temperature for 3 h in air. The sample was then cooled to room temperature in the furnace. OHAp single crystals were separated from the solidified flux by mechanically breaking up large clumps and washing with hot (90 °C) water, followed by rinsing with methanol and acetone.

Chloroapatite (ClAp) and fluorapatite (FAp) single crystals were synthesized using a calcium chloride/fluoride flux.[51] For ClAp, CaCl$_2$, and Ca$_3$(PO$_4$)$_2$ powders were mixed with a porcelain mortar and pestle in a molar ratio of 3.33:1 (5.5 g of CaCl$_2$ and 4.65 g of Ca$_3$(PO$_4$)$_2$), placed in a 25 mL alumina crucible, and covered loosely with an alumina cover. The mixture was heated to 1375 °C (5.7 °C/min) and held at this temperature for 15 h in air. The sample was cooled slowly to 1220 °C (3 °C/h), and then cooled to room temperature in the furnace. The sample was washed with boiling water by vacuum filtration to remove CaCl$_2$ flux.

For FAp single crystal synthesis, CaF$_2$ and Ca$_3$(PO$_4$)$_2$ were mixed together at a molar ratio of 3.33:1 with a porcelain mortar and pestle (230 mg of CaF$_2$ and 280 mg of Ca$_3$(PO$_4$)$_2$) and placed in a 1 mL tungsten evaporation boat. The mixture was heated to 1375 °C (5.7 °C/min) and held at this temperature for 15 h under a constant flow of nitrogen gas. It was cooled slowly to 1220 °C (3 °C/h), and then cooled to room temperature in the furnace. Excess calcium fluoride flux was removed by boiling in an aqueous solution of aluminum nitrate (10 wt % (Al(NO$_3$)$_3$·9H$_2$O). The recovered sample was washed with water repeatedly by vacuum filtration. The crystallinity and phase purity of all synthesized apatites were verified by X-ray diffraction, Raman spectroscopy, and Fourier transform infrared spectroscopy.

X-ray Powder and Single Crystal Diffraction. Synthetic OHAp and ClAp and geological fluorapatite (geoFAp) single crystals were ground to a fine powder with an agate mortar and pestle. Powders were loaded into a clean quartz sample holder with a 0.2 mm deep cavity, flattened with a glass microscope slide, and fixed in place with a mixture of hairspray and isopropyl alcohol. Powder diffraction patterns were recorded using Cu−Kα radiation in a D-Max X-ray diffractometer (Rigaku, The Woodlands, TX). The 2θ angle was scanned from 15° and 70° with a step size of 0.04° and a dwell time of 2 s. Diffraction patterns (Supporting Information Figures 5−7) are consistent with patterns simulated using CrystalDiffract (CrystalMaker Software Limited, Begbroke, Oxfordshire, UK) and published crystal structures.[10]

Unit cell parameters of a synthetic FAp crystal were determined by single-crystal X-ray diffraction at the Northwestern Integrated Molecular Structure Education and Research Center (IMSERC) using a Platform APEX II (Bruker, Madison, WI) equipped with a Mo X-ray source. Experimental values ($a = b$ = 9.3886 ± 0.0202 Å, c = 6.9060 ± 0.0148 Å, $\alpha = \beta$ = 90° and γ = 120°) are consistent with the literature values for ($a = b$ = 9.3973, c = 6.8782, $\alpha = \beta$ = 90° and γ = 120°).[10]

Reflectance Fourier Transform Infrared Spectroscopy. Samples were analyzed using a Tensor 37 FT-IR (NIR/mid-IR, Bruker, Billerica MA) bench coupled with a HYPERION microscope equipped

with MCD detector and a 15× objective. Measurements were made in reflectance mode. Spectra were collected with 4 cm^{-1} spectral resolution from 7000 to 400 cm^{-1} (Supporting Information Figure 8). Phase purity was confirmed by FTIR and spectra are consistent with literature spectra.[52]

Raman Spectroscopy. Raman spectra were recorded in backscattering geometry using 532 nm excitation in a WITec alpha300R confocal Raman microscope (WITec Instruments Corp. Maryville, TN) with a spatial resolution of 0.7−1.6 μm and spectral resolution of 0.9 cm^{-1}. The laser power was set to 10−45 μW to minimize local heating of the sample. Integration times were 30−60 s. Spectra were calibrated against a silicon standard (Supporting Information Figure 9). Observed PO$_4$ ν_1, ν_2, ν_3, and ν_4 vibrational modes, lattice modes, and the OH$^-$ stretch were consistent with literature spectra.[53]

Dissection, Fixation, Dehydration, and Embedding. A central 5 mm long section of hind-left femur was removed with a bone saw and fixed in 2.5% gluteraldehyde in cacodylate buffer (100 mM, pH 7.4) overnight at 4 °C, dehydrated in a graded ethanol series (50, 75, 90, 100%) and defatted in chloroform. The dehydrated sample was infiltrated with LR white resin containing a benzoyl peroxide catalyst, and was subsequently polymerized overnight within a sealed gelatin capsule at 60 °C.

ClAp and FAp single crystals were embedded in Epo-Fix resin and polymerized overnight at 25 °C.

Grinding and Polishing. The embedded femur sample was cut transversely with a low speed diamond saw (Buehler Isomet, Lake Bluff, IL). All embedded samples were ground using progressively finer grits of SiC grinding paper (400, 600, 800, and 1200 grit) and polished using polycrystalline aqueous diamond polishing suspensions (6, 3, 1, and 0.1 μm) on Microcloth polishing cloths.

The elephant tusk dentin sample was received as a polished geological thin section mounted on a glass slide. The age at death estimated 53 ± 5 years based on the wear pattern of last lower molar.

Polished samples were secured to an aluminum stub with cyanoacrylate adhesive, coated with ~25 nm of Pt with an ion beam sputter deposition and etching system (IBS/e, South Bay Technologies, San Clemente, CA) operating at a base pressure of <10^{-4} Pa, a working pressure of 10^{-2} Pa argon, with two ion guns operating at 8 kV at 3 mA per gun. The coating was grounded to the stub with conductive liquid silver paint.

APT Sample Preparation. Samples for APT were prepared using the SEM/FIB instrument (Helios Nanolab, FEI, Hillsboro, Oregon) using established protocols.[54,55] A rectangle of platinum (FIB-Pt) was deposited on the polished cross-section using the ion beam (30 kV, 93pA) to decompose methyl cyclopentadienyl trimethyl platinum ([C$_5$H$_5$Pt(CH$_3$)$_3$]) gas, over a region of interest (2 × 25 μm) on the polished cross sections or directly on faceted crystals. A wedge of material below the Pt rectangle was cut out on three sides using the FIB (30 kV, 6.5 nA). The wedge was attached to an *in situ* nanomanipulator (Omniprobe, Dallas, TX) using FIB-deposited Pt before cutting the final edge free. 1−2 μm wide segments were cut from the wedge and sequentially affixed to the tops of Si posts in an array (Cameca Scientific Instruments, Madison, WI) with FIB-Pt. Each tip was shaped and sharpened using annular milling patterns of increasingly smaller inner and outer diameters. The majority of the amorphized surface region and implanted gallium ions in the tip surface was removed by a final ion-milling step at 2 kV, 0.4 nA.

APT Methods. Atom probe tomographic analyses were conducted in a Cameca local-electrode atom-probe (LEAP 4000XSi, Cameca, Madison, WI) tomograph using a pulsed frequency-tripled Nd:YAG laser (λ = 355 nm). Run time parameters (200 kHz, 150 pJ per pulse) were optimized for OHAp as described in Supporting Information Figure 1. The DC potential on a microtip during APT was controlled to maintain an evaporation rate of either of 0.005 or 0.0025 ions per laser pulse. The base temperature of the microtip was maintained at 40 K and the ambient vacuum pressure was <10^{-8} Pa. Peak ranges were defined as the entire visible peak, and background was corrected by sideband subtraction.[56]

Three-dimensional reconstruction of APT data was performed using the Cameca integrated visualization and analysis

software (IVAS) based on published algorithms, assuming a hemispherical tip shape.[23,57] Standard reconstruction parameters were used with an electric field dependent tip radius (r). The average evaporation field (F_e, 14 V·nm^{-1}) used for reconstruction of the data was determined from radius measurements on SEM or TEM images of microtips after APT analysis. The average ionic volume used for the reconstruction was calculated based on the average atomic volume (0.0129 nm^3), specifically, the volume of the OHAp unit cell (0.5279 nm^3) divided by the number of atoms in the OHAp unit cell (41, excluding hydrogen) based on a published crystal structure.[10] The ionic volume (0.0258 nm^3) was calculated as twice the atomic volume as a result of the formation of molecular ions (average: 2 atoms/ion). The detector efficiency parameter used in the reconstruction was adjusted to account for the large number of unranged hits (75%) in the data due to the large thermal tails.

Conflict of Interest: The authors declare no competing financial interest.

Supporting Information Available: Optimization of APT run-time parameters, complete list of detected ions, APT spectra, calcium-containing ion abundances, bone spectra, list of unknown bone/dentin ions, bone/dentin composition, XRD, FTIR, Raman spectroscopy. This material is available free of charge *via* the Internet at http://pubs.acs.org.

REFERENCES AND NOTES

1. Boskey, A. Bone Mineral Crystal Size. *Osteoporosis Int.* **2003**, *14*, 16–21.
2. Fratzl, P.; Gupta, H.; Paschalis, E.; Roschger, P. Structure and Mechanical Quality of the Collagen–Mineral Nano-Composite in Bone. *J. Mater. Chem.* **2004**, *14*, 2115–2123.
3. Launey, M. E.; Buehler, M. J.; Ritchie, R. O. On the Mechanistic Origins of Toughness in Bone. *Annu. Rev. Mater. Res.* **2010**, *40*, 25–53.
4. Campbell, A.; LoRe, M.; Nancollas, G. The Influence of Carbonate and Magnesium Ions on the Growth of Hydroxyapatite, Carbonated Apatite and Human Powdered Enamel. *Colloids Surf.* **1991**, *54*, 25–31.
5. Kohn, M. J.; Rakovan, J.; Hughes, J. M. *Phosphates: Geochemical, Geobiological and Materials Importance*; Minerological Society of America Geochemical Society: Washington, DC, 2002; Vol. 48, p 742.
6. Kreidler, E.; Hummel, F. The Crystal Chemistry of Apatite: Structure Fields of Fluor-and Chlorapatite. *Am. Mineral.* **1970**, *55*, 170–184.
7. Jaffe, W. L.; Scott, D. F. Current Concepts Review—Total Hip Arthroplasty with Hydroxyapatite-Coated Prostheses. *J. Bone Joint Surg.* **1996**, *78*, 1918–34.
8. Waychunas, G. A. Apatite Luminescence. *Rev. Mineral. Geochem.* **2002**, *48*, 701–742.
9. Wopenka, B.; Pasteris, J. D. A Mineralogical Perspective on the Apatite in Bone. *Mater. Sci. Eng., C* **2005**, *25*, 131–143.
10. Hughes, J. M.; Cameron, M.; Crowley, K. D. Structural Variations in Natural F, OH, and Cl Apatites. *Am. Mineral.* **1989**, *74*, 870.
11. Glimcher, M. J. Bone: Nature of the Calcium Phosphate Crystals and Cellular, Structural, and Physical Chemical Mechanisms in Their Formation. *Rev. Mineral. Geochem.* **2006**, *64*, 223–282.
12. Falini, G.; Albeck, S.; Weiner, S.; Addadi, L. Control of Aragonite or Calcite Polymorphism by Mollusk Shell Macromolecules. *Science* **1996**, *271*, 67.
13. Robinson, C.; Shore, R.; Brookes, S.; Strafford, S.; Wood, S.; Kirkham, J. The Chemistry of Enamel Caries. *Crit. Rev. Oral Biol. Med.* **2000**, *11*, 481–495.
14. Bergstrom, W. H.; Wallace, W. M. Bone as a Sodium and Potassium Reservoir. *J. Clin. Investig.* **1954**, *33*, 867.
15. Copp, D. H.; Shim, S. The Homeostatic Function of Bone as a Mineral Reservoir. *Oral Surg. Oral Med. Oral Pathol.* **1963**, *16*, 738–744.
16. Hu, Y. Y.; Rawal, A.; Schmidt-Rohr, K. Strongly Bound Citrate Stabilizes the Apatite Nanocrystals in Bone. *Proc. Natl. Acad. Sci. U.S.A.* **2010**, *107*, 22425–22429.
17. Roelofs, A. J.; Ebetino, F. H.; Reszka, A. A.; Russel, R. G. G.; Rogers, M. J. Bisphosphonates. In *Principles of Bone Biology*, 3rd ed.; Bilezikian, J. P., Raisz, L. G., Martin, T. J., Eds.; Elsevier/Academic Process: Amsterdam, Boston, 2008; pp 1737–1767.
18. Featherstone, J. D. B. Prevention and Reversal of Dental Caries: Role of Low Level Fluoride. *Community Dent. Oral Epidemiol.* **1999**, *27*, 31–40.
19. Krishnamachari, K. Skeletal Fluorosis in Humans: A Review of Recent Progress in the Understanding of the Disease. *Prog. Food Nutr. Sci.* **1986**, *10*, 279.
20. Andress, D. L.; Maloney, N. A.; Endres, D. B.; Sherrard, D. J. Aluminum-Associated Bone Disease in Chronic Renal Failure: High Prevalence in a Long-Term Dialysis Population. *J Bone Miner. Res.* **1986**, *1*, 391–398.
21. Gordon, L. M.; Joester, D. Nanoscale Chemical Tomography of Buried Organic–Inorganic Interfaces in the Chiton Tooth. *Nature* **2011**, *469*, 194–197.
22. Joester, D.; Hillier, A.; Zhang, Y.; Prosa, T. J. Organic Materials and Organic/Inorganic Heterostructures in Atom Probe Tomography. *Microsc. Today* **2012**, *20*, 26–31.
23. Miller, M. K. *Atom Probe Tomography: Analysis at the Atomic Level*; Springer: New York, 2000.
24. Kelly, T. F.; Miller, M. K. Invited Review Article: Atom Probe Tomography. *Rev. Sci. Instrum.* **2007**, *78*, 031101.
25. Kuhlman, K.; Martens, R.; Kelly, T.; Evans, N.; Miller, M. Fabrication of Specimens of Metamorphic Magnetite Crystals for Field Ion Microscopy and Atom Probe Microanalysis. *Ultramicroscopy* **2001**, *89*, 169–176.
26. McMurray, S.; Gorman, B.; Diercks, D. Tem and Atom Probe Investigation of Calcium Carbonate Precipitation in Seawater. *Microsc. Microanal.* **2011**, *17*, 759.
27. Chen, Y.; Ohkubo, T.; Hono, K. Laser Assisted Field Evaporation of Oxides in Atom Probe Analysis. *Ultramicroscopy* **2011**, *111*, 562–566.
28. Larson, D.; Alvis, R.; Lawrence, D.; Prosa, T.; Ulfig, R.; Reinhard, D.; Clifton, P.; Gerstl, S.; Bunton, J.; Lenz, D. Analysis of Bulk Dielectrics with Atom Probe Tomography. *Microsc. Microanal.* **2008**, *14*, 1254–1255.
29. Pauling, L. The Nature of the Chemical Bond. *J. Chem. Educ.* **1992**, *69*, 519.
30. Kellogg, G. L. Field Ion Microscope Studies of Single-Atom Surface Diffusion and Cluster Nucleation on Metal Surfaces. *Surf. Sci. Rep.* **1994**, *21*, 1–88.
31. Chiba, T.; Nojima, M.; Owari, M. Improvement of a Method for Reconstructing the Three-Dimensional Atom Probe (3DAP) Data. *Surf. Interface Anal.* **2006**, *38*, 1751–1755.
32. Weiner, S.; Wagner, H. D. The Material Bone: Structure–Mechanical Function Relations. *Annu. Rev. Mater. Sci.* **1998**, *28*, 271–298.
33. Elliott, J. C. Calcium Phosphate Biominerals. *Rev. Mineral. Geochem.* **2002**, *48*, 427–453.

34. Nriagu, J. O.; Moore, P. B. *Phosphate Minerals*; Springer-Verlag: Berlin, 1984.

35. Xie, B.; Nancollas, G. H. How to Control the Size and Morphology of Apatite Nanocrystals in Bone. *Proc. Natl. Acad. Sci. U.S.A.* **2010**, *107*, 22369–22370.

36. Weiner, S.; Traub, W. Bone Structure: From Angstroms to Microns. *FASEB J.* **1992**, *6*, 879–885.

37. Landis, W. J. Mineral Characterization in Calcifying Tissues: Atomic, Molecular and Macromolecular Perspectives. *Connect. Tissue Res.* **1996**, *34*, 239–246.

38. Landis, W.; Song, M.; Leith, A.; McEwen, L.; McEwen, B. Mineral and Organic Matrix Interaction in Normally Calcifying Tendon Visualized in Three Dimensions by High-Voltage Electron Microscopic Tomography and Graphic Image Reconstruction. *J. Struct. Biol.* **1993**, *110*, 39–54.

39. Jantou-Morris, V.; Horton, M. A.; McComb, D. W. The Nano-morphological Relationships between Apatite Crystals and Collagen Fibrils in Ivory Dentine. *Biomaterials* **2010**, *31*, 5275–5286.

40. Märten, A.; Fratzl, P.; Paris, O.; Zaslansky, P. On the Mineral in Collagen of Human Crown Dentine. *Biomaterials* **2010**, *31*, 5479–5490.

41. McNally, E. A.; Schwarcz, H. P.; Botton, G. A.; Arsenault, A. L. A Model for the Ultrastructure of Bone Based on Electron Microscopy of Ion-Milled Sections. *PLoS One* **2012**, *7*, e29258.

42. Greene, M.; Prosa, T.; Larson, D.; Kelly, T. Focused Ion Beam Fabrication of Solidified Ferritin into Nanoscale Volumes for Compositional Analysis Using Time-of-Flight Mass Spectrometry Methods. *Microsc. Microanal.* **2010**, *16*, 1860–1861.

43. Cui, F. Z.; Li, Y.; Ge, J. Self-Assembly of Mineralized Collagen Composites. *Mater. Sci. Eng.: Rep.* **2007**, *57*, 1–27.

44. Orgel, J. P. R. O.; Irving, T. C.; Miller, A.; Wess, T. J. Micro-fibrillar Structure of Type I Collagen *in Situ*. *Proc. Natl. Acad. Sci. U.S.A.* **2006**, *103*, 9001–9005.

45. Ji, B.; Gao, H. Mechanical Properties of Nanostructure of Biological Materials. *J. Mech. Phys. of Solids* **2004**, *52*, 1963–1990.

46. Jantou, V.; Turmaine, M.; West, G.; Horton, M.; McComb, D. Focused Ion Beam Milling and Ultramicrotomy of Mineralised Ivory Dentine for Analytical Transmission Electron Microscopy. *Micron* **2009**, *40*, 495–501.

47. Cui, F.; Wen, H.; Zhang, H.; Ma, C.; Li, H. Nanophase Hydroxyapatite-Like Crystallites in Natural Ivory. *J. Mater. Sci. Lett.* **1994**, *13*, 1042–1044.

48. Endcaps are the intersection between the isosurface and the edge of the rendered subvolume.

49. Vurpillot, F.; Bostel, A.; Blavette, D. Trajectory Overlaps and Local Magnification in Three-Dimensional Atom Probe. *Appl. Phys. Lett.* **2000**, *76*, 3127–3129.

50. Tas, A. C. Molten Salt Synthesis of Calcium Hydroxyapatite Whiskers. *J. Am. Ceram. Soc.* **2001**, *84*, 295–300.

51. Prener, J. S. The Growth and Crystallographic Properties of Calcium Fluor- and Chlorapatite Crystals. *J. Electrochem. Soc.* **1967**, *114*, 77–83.

52. Siddall, R.; Hurford, A. J. Semi-quantitative Determination of Apatite Anion Composition for Fission-Track Analysis Using Infra-red Microspectroscopy. *Chem. Geol.* **1998**, *150*, 181–190.

53. O'Shea, D.; Bartlett, M.; Young, R. Compositional Analysis of Apatites with Laser-Raman Spectroscopy: (OH, F, Cl) Apatites. *Arch. Oral Biol.* **1974**, *19*, 995–1006.

54. Miller, M. K.; Russell, K. F.; Thompson, G. B. Strategies for Fabricating Atom Probe Specimens with a Dual Beam FIB. *Ultramicroscopy* **2005**, *102*, 287–298.

55. Thompson, K. F.; Lawrence, D. F.; Larson, D. J.; Olson, J. D.; Kelly, T. F.; Gorman, B. *In Situ* Site-Specific Specimen Preparation for Atom Probe Tomography. *Ultramicroscopy* **2007**, *107*, 131–139.

56. Oltman, E.; Ulfig, R.; Larson, D. Background Removal Methods Applied to Atom Probe Data. *Microsc. Microanal.* **2009**, *15*, 256–257.

57. Bas, P.; Bostel, A.; Deconihout, B.; Blavette, D. A General Protocol for the Reconstruction of 3D Atom Probe Data. *Appl. Surf. Sci.* **1995**, *87*, 298–304.